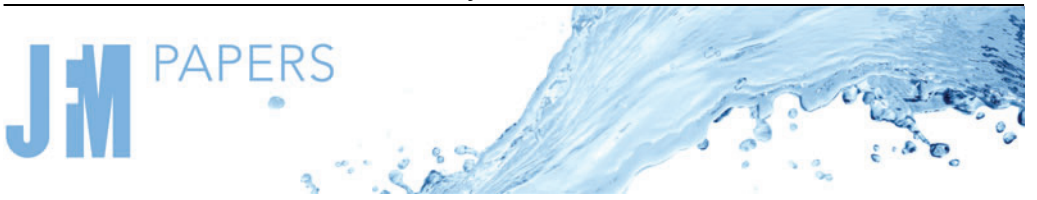
J. Fluid Mech. (2025), *vol*. 1002, A32, doi:10.1017/jfm.2024.1164



Inverse Leidenfrost impacting drops

Kindness Isukwem[1], Carole-Ann Charles[2], Ty Phou[2], Laurence Ramos[2], Christian Ligoure[2], Elie Hachem[1] and Anselmo Pereira[1],†

[1]Mines Paris, PSL University, Centre for Material Forming (CEMEF), UMR CNRS 7635, rue Claude Daunesse, 06904 Sophia-Antipolis, France

[2]Laboratoire Charles Coulomb (L2C), Université de Montpellier, CNRS, 34090 Montpellier, France

(Received 31 December 2023; revised 5 November 2024; accepted 11 November 2024)

We investigate the spreading of falling ambient-temperature Newtonian drops after their normal impact on a quartz plate covered with a thin layer of liquid nitrogen. As a drop expands, liquid nitrogen evaporates, generating a vapour film that maintains the drop in levitation. Consequently, the latter spreads in inverse Leidenfrost conditions. Three drop-spreading regimes are observed: (i) inertio-capillary, (ii) inertio-viscous, and (iii) inertio-viscous-capillary. In the first regime, although the drop expansion is essentially driven by a competition between inertial and capillary stresses, it is also affected by viscous effects emerging from the vapour film, which ultimately favours the development of a shear flow within the drop. Interestingly, vapour film effects become marginal in both the second and third regimes, allowing the drop to undergo biaxial extension primarily. More specifically, in the inertio-viscous scenario, the expansion is driven by the balance between inertial and biaxial extensional viscous stresses in the drop. Finally, inertia, capillarity and drop viscosity are all relevant in the third regime. These physical mechanisms are underlined through a mixed approach combining experiments with multiphase three-dimensional numerical simulations in light of spreading dynamics analyses, energy transfer and scaling laws. Our results are rationalized in a two-dimensional diagram linking the drops' maximum expansion and spreading time with the observed spreading regimes through a single dimensionless parameter given by the square root of the capillary number (the ratio of the viscous stress to the capillary stress).

Key words: drops

1. Introduction

The spreading of Newtonian drops impacting on solid surfaces (Worthington 1883; Roisman *et al.* 2002; Clanet *et al.* 2004; Lee *et al.* 2015) has received significant attention in the literature, being the subject of many review articles (Rein 1993; Yarin 2006;

† Email address for correspondence: anselmo.soeiro_pereira@mines-paristech.fr

© The Author(s), 2025. Published by Cambridge University Press

https://doi.org/10.1017/jfm.2024.1164 Published online by Cambridge University Press

Josserand & Thoroddsen 2016). Variants of this problem have been explored as well, such as the impact of non-Newtonian drops (Crooks & Boger 2000; Cooper-White, Crooks & Boger 2002; Luu & Forterre 2009, 2014; Boyer *et al.* 2016; Oishi, Thompson & Martins 2019; Isukwem *et al.* 2024*b*,*c*), the drop impact onto inclined planes (Laan *et al.* 2014; LeClear *et al.* 2016), onto a target (Arora, Ligoure & Ramos 2016; Arora *et al.* 2021), onto a permeable body or a mesh (Lorenceau & Quéré 2003; Soto *et al.* 2018; Su *et al.* 2020), the drop impact on a thin horizontal fibre (Lorenceau, Clanet & Quéré 2004; Comtet, Keshavarz & Bush 2016), on a liquid film (Blackwell *et al.* 2015; Guo & Lian 2018), and the drop–drop collision (Ramírez-Soto *et al.* 2020). These flow configurations are intrinsically associated with multiple applied processes, including forensic science, atomization, spray coating, firefighting, inkjet printing, and more recently three-dimensional (3-D) printing of electronic components, organs, tissues and prosthetics (Bordoloi & Longmire 2014; Laan *et al.* 2014; Murphy & Atala 2014; Ryu *et al.* 2017; Kumar *et al.* 2018; Vijayavenkataraman *et al.* 2018; Modak *et al.* 2020).

In the mentioned applications, the control of the drop-spreading dynamics emerges from a delicate balance between inertial, interfacial and viscous stresses. Furthermore, the drop expansion is also affected by interactions between the impacting object and the impacted substrate (Quéré 2008; Bonn *et al.* 2009; Duez *et al.* 2010; Carlson, Do-Quang & Amberg 2011; Josserand & Thoroddsen 2016), and it is strongly facilitated by the use of repellent surfaces, such as superhydrophobic ones (Richard, Clanet & Quéré 2002; Clanet *et al.* 2004; Josserand & Thoroddsen 2016; Quetzeri-Santiago *et al.* 2019), and plates heated above the Leidenfrost temperature (Leidenfrost 1756; Garmett 1878; Biance, Clanet & Quéré 2003; Lee *et al.* 2020; Graeber *et al.* 2021; Wang *et al.* 2022). In this connection, an essential and scarcely explored flow scenario regards the impact of a drop onto a solid surface in inverse Leidenfrost conditions (Hall *et al.* 1969; Adda-Bedia *et al.* 2016; Gauthier *et al.* 2019), i.e. the solid surface is covered with a thin layer of liquid nitrogen that partially evaporates as the drop expands after its impact. The generated vapour film prevents the drop's contact with both the liquid nitrogen and the solid plate, favouring the spread of the impacting object. In such a scenario, the levitating drop would experience a biaxial extensional deformation, a point discussed in very few works in the literature (Arora *et al.* 2018; Louhichi *et al.* 2020; Charles *et al.* 2021) that deserves deeper investigations. Attempts to extend the existing analyses should then naturally contemplate the physical mechanisms governing the drop spreading for a wide range of viscosity, surface tension, density and impact velocity.

In the present work, we investigate the spreading of falling ambient-temperature Newtonian drops, after their normal impact on a solid plate covered with a thin layer of liquid nitrogen. Due to the temperature difference between a drop and the liquid nitrogen, the latter partially evaporates, generating a vapour film that maintains the drop in levitation as it expands. This is the inverse Leidenfrost effect. We extend previous studies on this phenomenon by highlighting the physical mechanisms driving the spreading of the levitating drops after their impact. Three spreading regimes are observed: (i) inertio-capillary (balancing inertial and capillary stresses); (ii) inertio-viscous (balancing inertial and viscous stresses); and (iii) inertio-viscous-capillary (for which inertia, capillarity and viscosity are all relevant). These regimes are underlined through a mixed approach combining experiments and 3-D numerical simulations based on an adaptive variational multi-scale method for two fluids (the drop and the surrounding nitrogen vapour). Experimental and numerical results are explored in light of spreading dynamics analyses, energy transfer, and scaling laws for the drops' maximum diameter and spreading time.

https://doi.org/10.1017/jfm.2024.1164 Published online by Cambridge University Press

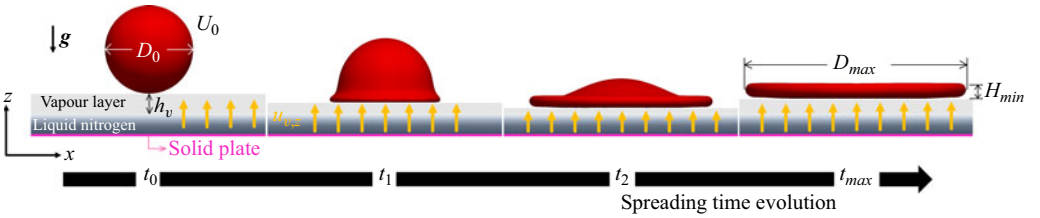


Figure 1. An ambient-temperature Newtonian drop (in red) of initial diameter D_0, density ρ, and viscosity η falls by gravity g and impacts at the instant t_0 with velocity U_0 a solid plate (in magenta) covered with a thin layer of liquid nitrogen (in dark blue) at temperature T_l. As the drop expands, liquid nitrogen evaporates, generating a vapour film (in grey) of thickness h_v, density ρ_v, viscosity η_v, and normal velocity $u_{v,z}$ that maintains the drop in levitation. Hence the latter spreads in inverse Leidenfrost conditions until achieving its maximum diameter D_{max} and minimal thickness H_{min} at the instant t_{max}.

The organization of the paper is as follows. A detailed description of the physical formulation and the mixed experimental–numerical method is presented in § 2. Experimental and numerical results are discussed in § 3. Finally, conclusions and perspectives are drawn § 4.

2. Problem statement, mixed experimental–numerical approach, and relevant dimensionless parameters

2.1. *Problem statement*

As illustrated in figure 1, we consider the spreading time evolution of an ambient-temperature Newtonian falling drop (in red) of initial diameter D_0, density ρ, and viscosity η, after it impacts at the instant t_0 with velocity U_0 a solid plate (in magenta) covered with a thin layer of liquid nitrogen (in dark blue) at temperature T_l. As the drop expands, liquid nitrogen evaporates, generating a vapour film (in grey) of thickness h_v, density ρ_v, viscosity η_v, and normal velocity $u_{v,z}$ that maintains the drop in levitation. Consequently, the latter spreads in inverse Leidenfrost conditions until achieving its maximum diameter D_{max} and minimal thickness H_{min} at the instant t_{max}. Surface tension between the drop and the surrounding gases is denoted by σ.

The dynamics regarding the eventual retraction of the drop induced by surface tension effects is out of the scope of the present work. Splashing events are not taken into account either. More specifically, for some of our experiments, we do observe azimuthal instabilities and splashing, which are typically favoured by high impact velocities, low drop viscosities, and low surface tensions. These instabilities are equally captured by our numerical simulations. Nevertheless, their development will be a matter of future works. Hence results involving splashing events were excluded from the data presented in § 3.

2.2. *Mixed experimental–numerical approach*

As schematized in figure 2(*a*), the impact and spreading events are experimentally recorded simultaneously by two high-speed cameras: (1) from the top by a Phantom V 7 : 3 operated at 6700 fps with resolution 800×600 pixels^2, where the angle between the camera axis and the vertical plane is approximately 10°); and (2) from the side by a Phantom Miro M310 operated at 3200 fps with resolution 1280×800 pixels^2. An LED backlight system provides the necessary lighting level. The millimetric drop of temperature T_0 varying between 18.5 °C and 22.5 °C falls by gravity from a nozzle and hits a solid quartz plate (in magenta) covered with a thin liquid nitrogen layer (in blue) at temperature

https://doi.org/10.1017/jfm.2024.1164 Published online by Cambridge University Press

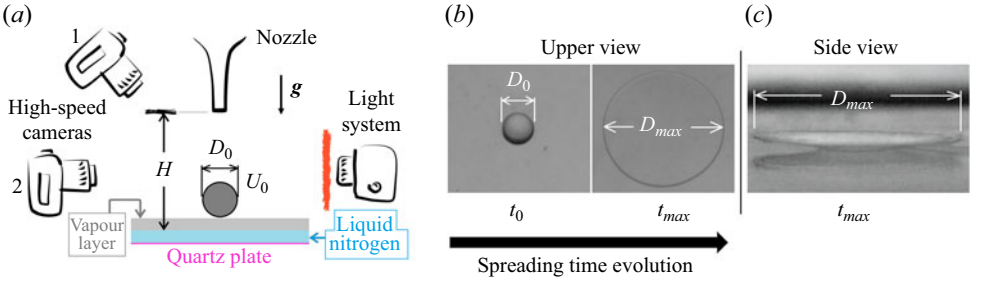


Figure 2. (*a*) Schematic illustration of the experimental set-up for the investigation of the impacting drops in an inverse Leidenfrost situation. The millimetric drop falls by gravity from a nozzle and hits a solid quartz plate (in magenta) covered with a thin layer of liquid nitrogen (in blue), which partially evaporates, generating a vapour film (in grey) that maintains the drop in levitation during its spreading. The impact events are experimentally recorded simultaneously by two high-speed cameras: (1) from the top; and (2) from the side. Typical snapshots captured by the top-view and the side-view cameras are shown in (*b*,*c*), respectively.

$T_l = -196\,^{\circ}\mathrm{C}$, which partially evaporates. (Details on the experimental set-up are given in Arora *et al.* 2018.) Due to the temperature difference ΔT between the drop and the liquid nitrogen, heat diffuses through the vapour phase, vaporizing part of the liquid nitrogen. The escaping vapour (in grey) of normal velocity $u_{v,z}$ is then confined below the drop within a thin film of thickness h_v, and lubrication generates an overpressure that sustains the drop in levitation during its spreading (values of h_v and $u_{v,z}$ are detailed at the end of this subsection). Typical snapshots captured by the top-view and side-view cameras are shown in figures 2(*b*) and 2(*c*), respectively. The time evolution of the sheet size is measured with ImageJ software by analysing top-view images. We first subtract the background image from the expansion movie and highlight the rim by binary thresholding. This allows us to determine the sheet's contour and measure its area A as a function of time. An apparent instantaneous sheet's diameter is simply deduced as $D = \sqrt{4A/\pi}$.

Initial drop diameters D_0 are in the range 3.5–5 mm, and the experimental impact velocity U_0 varies from 3 m s^{-1} to 4.25 m s^{-1}. Glycerol–water mixtures ($1050 \leqslant \rho \leqslant 1260$ kg m^{-3}, $0.00105 \leqslant \eta \leqslant 1.91$ Pa s, $\sigma = 68$ mN m^{-1}) and silicone oils ($913 \leqslant \rho \leqslant 970$ kg m^{-3}, $0.0052 \leqslant \eta \leqslant 5$ Pa s, $\sigma = 20$ mN m^{-1}) are used.

Our computational approach is based on a general solver (CIMLIB-CFD, a parallel, finite-element library; Coupez & Hachem 2013) that takes into account the rheological behaviour of two fluid phases (the drop and the nitrogen vapour; the liquid nitrogen phase is not considered here), as well as surface tension effects (Riber *et al.* 2016; Pereira *et al.* 2019; Valette *et al.* 2019, 2021; Pereira, Hachem & Valette 2020; Isukwem, Hachem & Pereira 2024*a*; Isukwem *et al.* 2024*b*,*c*). More precisely, the momentum equation applied to the considered solenoidal flows ($\boldsymbol{\nabla} \cdot \boldsymbol{u} = 0$) reads

$$\rho\left(\frac{\partial \boldsymbol{u}}{\partial t} + \boldsymbol{u} \cdot \boldsymbol{\nabla}\boldsymbol{u} - \boldsymbol{g}\right) = -\boldsymbol{\nabla} p + \boldsymbol{\nabla} \cdot \boldsymbol{\tau} + \boldsymbol{f}_{st}, \tag{2.1}$$

in which $\boldsymbol{u}$, p, $\boldsymbol{\tau}$, $\boldsymbol{\nabla}$, $\boldsymbol{g}$, $\boldsymbol{\nabla}\cdot$ and $\boldsymbol{f}_{st}$ are, respectively, the velocity vector $\boldsymbol{u} = \{u_x, u_y, u_z\}$, the pressure, the extra-stress tensor, the gradient operator, the gravity vector, the divergence operator, and a capillary term related to the surface tension force. The latter is defined as $\boldsymbol{f}_{st} = -\sigma\kappa\Phi\boldsymbol{n}$, where σ, κ, Φ and $\boldsymbol{n}$ are the drop surface tension with the surrounding gas, the curvature of the drop–gas interface, the Dirac function locating the liquid–gas interface, and its normal vector, respectively. In addition, the extra-stress tensor is given

https://doi.org/10.1017/jfm.2024.1164 Published online by Cambridge University Press

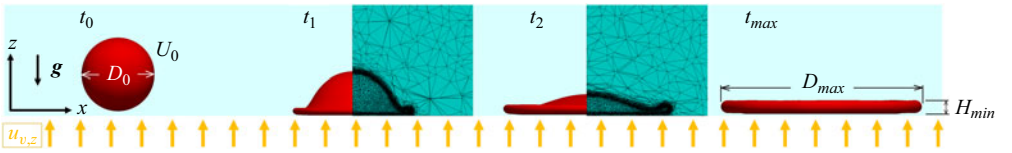


Figure 3. Numerical configuration taken into account. The drop (in red) of diameter D_0 falls by gravity $\boldsymbol{g}$ and reaches the velocity U_0 at t_0, after which it expands in levitation induced by the action of a vapour (in blue) counter-flow whose inlet vertical velocity $u_{v,z}$ is imposed at the bottom wall of the computational domain (yellow arrows). At the instant t_{max}, the drop achieves its maximum diameter D_{max} and a minimum height H_{min}. The spreading time evolution is represented by four snapshots. The used mesh (composed of approximately 10^6 elements) adapted around each interface (drop in red and vapour in blue) is illustrated by the black lines in the second and third snapshots.

by $\boldsymbol{\tau} = \eta\dot{\boldsymbol{\gamma}}$, in which $\dot{\boldsymbol{\gamma}}$ represents the rate-of-strain tensor defined as $\dot{\boldsymbol{\gamma}} = \boldsymbol{\nabla u} + \boldsymbol{\nabla u}^{\mathrm{T}}$. The norm of $\dot{\boldsymbol{\gamma}}$ is called the deformation rate, being defined as $\|\dot{\boldsymbol{\gamma}}\| = (\frac{1}{2}\dot{\boldsymbol{\gamma}} : \dot{\boldsymbol{\gamma}})^{1/2}$. Our numerical methods are based on a variational multi-scale approach combined with anisotropic mesh adaptation with highly stretched elements (Riber *et al.* 2016; Pereira *et al.* 2019, 2020; Valette *et al.* 2019, 2021; Isukwem *et al.* 2024*a*,*b*,*c*). The time evolution of the drop–gas interface is captured using a level-set function (Hachem *et al.* 2016). Fluid properties are interpolated through the level-set function whose value varies from positive within the drop to negative in the vapour (and zero at the interfaces between the different fluid phases). Supplemental details concerning the interface capturing and the level-set function are available in Appendix A.

The 3-D numerical configuration taken into account is illustrated in figure 3. Four numerical snapshots show the spreading time evolution. Only the drop (in red) and the vapour phase (in blue) are considered. The mesh (composed of approximately 10^6 elements; see black lines on the right-hand side of the second and third snapshots) is adapted around each interface. The corresponding zero isovalues for the level-set function are also shown (in red). The considered numerical drops are millimetric, $3 \leqslant D_0 \leqslant 10$ mm. Furthermore, wide ranges of liquid properties are explored numerically: $250 \leqslant \rho \leqslant 2500$ kg m^{-3}, $0.001 \leqslant \eta \leqslant 10$ Pa s, $0.005 \leqslant \sigma \leqslant 1$ N m^{-1}. The numerical impact velocity varies from 1 m s^{-1} to 5 m s^{-1}. Concerning the nitrogen vapour phase (in blue), both viscosity η_v and density ρ_v are constant at respectively 1.74×10^{-5} Pa s and 1.25 kg m^{-3}. Initial and boundary conditions for the flow equations are: initial vertical impact velocity U_0 within the drop; $\boldsymbol{u}_v = \{0, 0, u_{v,z}\}$ for the vapour phase at the bottom wall (normal inlet velocity represented by yellow arrows in figure 3); and zero normal stress in the other walls of the domain.

The normal velocity of the nitrogen vapour $u_{v,z}$ imposed as a boundary condition at the bottom wall (yellow arrows in figure 3) is calculated by assuming that the energy related to vaporization is brought by the thermal conduction through the vapour film induced by the temperature difference between the drop and the liquid nitrogen:

$$L_v \frac{\mathrm{d}m_v}{\mathrm{d}t} \sim K_v D^2 \frac{\Delta T}{h_v}, \tag{2.2}$$

in which L_v is the nitrogen latent heat of vaporization, $\mathrm{d}m_v/\mathrm{d}t$ is the rate of evaporation (mass per unit time), K_v is the thermal conductivity of vapour, and D is the instantaneous diameter of the drop. Since $\mathrm{d}m_v/\mathrm{d}t \sim \rho_v D^2 u_{v,z}$, the normal inlet velocity of the nitrogen

https://doi.org/10.1017/jfm.2024.1164 Published online by Cambridge University Press

vapour reads

$$u_{v,z} \sim \frac{K_v}{\rho_v L_v} \frac{\Delta T}{h_v}. \tag{2.3}$$

This equation is imposed as the normal inlet velocity of the nitrogen vapour at the bottom wall, with h_v being defined numerically as the smallest distance between the drop and the bottom wall at each time step (hence $u_{v,z}$ increases as the drop moves downwards, diminishing h_v).

The size of the smallest mesh elements in our numerical domain is taken as ten times smaller than the minimum h_v reached during the drop-spreading process $h_{v,min}$. Such a value is estimated by using lubrication theory. More specifically, the pressure variation within the vapour film given by the lubrication theory $\Delta p \sim \eta_v (u_{v,z}/h_v)(D^2/h_v^2)$ (Gauthier *et al.* 2019) is compared to the drop inertial stress at the impact $\sim \rho U_0^2$, leading to

$$u_{v,z} \sim \frac{\rho U_0^2 h_v}{\eta_v} \frac{h_v^2}{D^2}. \tag{2.4}$$

By combining (2.3) and (2.4), and taking $D = D_0$, we deduce an expression for $h_{v,min}$ as

$$h_{v,min} \sim \left(\frac{K_v \eta_v}{\rho_v L_v} \frac{D_0^2}{\rho U_0^2} \Delta T \right)^{1/4}, \tag{2.5}$$

leading to $h_{v,min} \sim O(10^1)$ μm (with $L_v = 2 \times 10^5$ J kg^{-1}, $K_v = 0.026$ W mK^{-1}, $\rho_v = 1.25$ kg m^{-3}, $\eta_v = 1.74 \times 10^{-5}$ Pa s), values of the same order of magnitude as those reported by Biance *et al.* (2003) and Gauthier *et al.* (2019) under static levitation conditions. Hence a minimal mesh size Δ_{min} of 1 μm is chosen (it is important to underline that this choice of Δ_{min} is also based on the supplemental numerical analyses presented in Appendix A).

For the impact events considered experimentally here, the drop reaches its maximum diameter D_{max} less than 10 ms after the beginning of the spreading process ($t_{max} < 10$ ms). In such a time interval, the heat exchange between the drop the nitrogen vapour is given by

$$-\rho D_0^3 c_p \frac{\mathrm{d}T}{\mathrm{d}t} \sim K_v D^2 \frac{T - T_l}{h_v}, \tag{2.6}$$

where c_p is the specific heat of the drop, and T is its instantaneous temperature. Consequently,

$$T \sim (T_0 - T_l) \exp\left(\frac{-K_v D^2 t}{\rho D_0^3 c_p h_v} \right) + T_l. \tag{2.7}$$

We find thus that the temperature of the drop at $t < 10$ ms is approximately equal to T_0 (with $c_p = 4181$ J kg^{-1} K^{-1}, $h_v = 10$ μm and $D < 6D_0$). For this reason, in our numerical simulations, the drop properties are considered constant throughout the spreading process.

Finally, note that liquid nitrogen and phase changes are not considered in our numerical framework. The expansion of the levitating drops in inverse Leidenfrost conditions is described exclusively through gravitational, inertial, capillary and viscous parameters related to the interactions between the drop and the nitrogen vapour. Nevertheless, we will show that such physical ingredients are sufficient to capture the main features observed in our experiments.

https://doi.org/10.1017/jfm.2024.1164 Published online by Cambridge University Press

2.3. *Relevant dimensionless numbers*

The important dimensionless quantities of the problem can be stressed by a classical dimensional analysis based on the Buckingham Π theorem with the physical system defined in terms of six physical variables (D_0, U_0, g, ρ, η, σ) that may be expressed in terms of three fundamental units, i.e. mass, length and time. The Buckingham Π theorem thus indicates that the system may be uniquely described in terms of three dimensionless groups:

$$Fr = \frac{\rho g D_0}{\rho U_0^2}, \quad Re = \frac{\rho U_0^2}{\eta (U_0/D_0)}, \quad We = \frac{\rho U_0^2}{\sigma / D_0}, \tag{2.8a–c}$$

where Fr is the Froude number, Re is the Reynolds number, and We is the Weber number. Since we consider here millimetric drops for which η and/or σ are relatively high, $\rho g D_0$ ends up playing a marginal role in comparison to the other stress terms, i.e. $Fr \leqslant 0.01$ (this will be shown in detail in the next section). Hence the particular flow scenarios explored here can be described by Re and We. Their roles on the spreading process will be highlighted in the next section.

3. Results and discussions

3.1. *Spreading dynamics*

Experimental and numerical top-view snapshots illustrating the time evolution of a silicone oil drop ($\rho = 955$ kg m^{-3}, $\eta = 0.658$ Pa s, $\sigma = 0.068$ N m^{-1}) impacting at $Re = 24.5$ and $We = 3432$ ($D_0 = 4$ mm, $U_0 = 4.25$ m s^{-1}) are displayed in figures 4(*a*) and 4(*b*), respectively. Following its impact at t_0, the drop expands, reaching $D_{max} = 11.7$ mm at $t_{max} = 4.5$ ms, and subsequently retracts via capillary stresses (see snapshots at $1.5t_{max}$). As indicated by numerical contours of the dimensionless radial velocity u_y/U_0 on the centre x–z plane shown by figure 4(*c*) at $0.25t_{max}$ (left-hand side) and $0.5t_{max}$ (right-hand side), during the spreading process the drop undergoes biaxial elongation. Such a result is equally pointed out by the radial variation exhibited by the corresponding dimensionless deformation rate contours $\|\dot{\boldsymbol{\gamma}}\|/(U_0/D_0)$ in figure 4(*d*). Similar outcomes are observed for all numerical simulations performed in the present work (not shown for brevity).

Further spreading dynamics analyses are illustrated in figure 5, in which the instantaneous dimensionless diameter $D(t)/D_0$ is plotted against the dimensionless time tU_0/D_0. The role of the Reynolds number on $D(t)/D_0$ is shown in figure 5(*a*), where experiments are represented by the solid symbols, while the numerical simulations are represented by the open ones. Each curve is related to a specific Re in the range 16.6–46.1 at $We = 3432$. As the inertia stress becomes more pronounced in comparison to the viscous stress, both the relative maximum spreading D_{max}/D_0 and the spreading time $t_{max}U_0/D_0$ increase. These quantities appear therefore as an increasing function of the Reynolds number (black arrow in figure 5*a*). An analogous tendency is observed in figure 5(*b*), where Weber number effects on $D(t)/D_0$ are stressed numerically at $Re = 161.5$ for $69 \leqslant We \leqslant 192$ (each curve being associated with a particular We), i.e. the enhancement of We leads to larger D_{max}/D_0 and $t_{max}U_0/D_0$ (black arrow in figure 5*b*).

3.2. *Energy transfer analyses*

The good agreement between experiments and simulations underlined by the above results gives us the confidence to explore numerically the physical mechanisms driving the spreading dynamics in light of energy transfer analyses. In figure 6, energy percentage curves related to the out-of-equilibrium inverse Leidenfrost system are plotted as a

https://doi.org/10.1017/jfm.2024.1164 Published online by Cambridge University Press

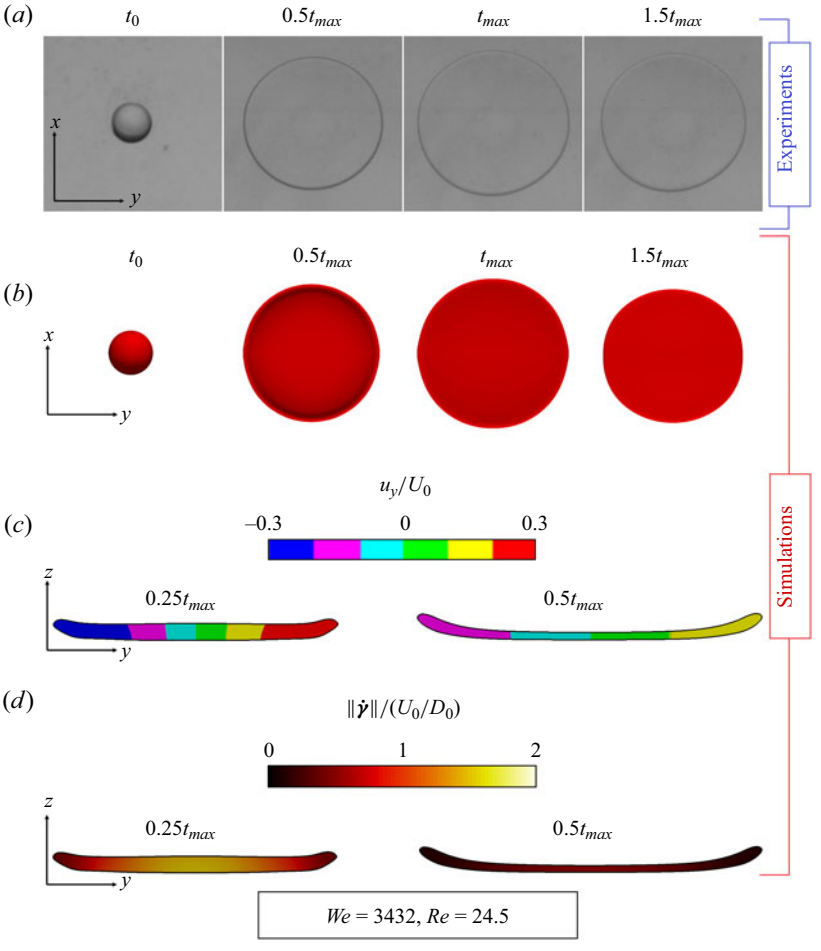


Figure 4. (*a*) Experimental and (*b*) numerical top-view snapshots illustrating the time evolution of a silicone oil drop ($\rho = 955$ kg m^{-3}, $\eta = 0.658$ Pa s, $\sigma = 0.020$ N m) impacting at $Re = 24.5$ and $We = 3432$ ($D_0 = 4$ mm, $U_0 = 4.25$ m s^{-1}). Following its impact at t_0, the drop expands, reaching $D_{max} = 11.7$ mm at $t_{max} = 4.5$ ms, and subsequently retracts via capillary stresses (see snapshots at $1.5t_{max}$). (*c*) Numerical contours of the dimensionless radial velocity u_y/U_0 on the centre x–z plane shown at $0.25t_{max}$ (left-hand side) and $0.5t_{max}$ (right-hand side). (*d*) Corresponding dimensionless deformation rate contours $\|\dot{\boldsymbol{\gamma}}\|/(U_0/D_0)$.

function of the dimensionless time: gravitational energy G, kinetic energy KE, surface energy SE (grey circles), and viscous dissipation W. These terms are defined as

$$\left.\begin{aligned} G = \int_V \rho g z \,\mathrm{d}V, \quad KE = \int_V \frac{1}{2}\,\rho\,\|\boldsymbol{u}\|^2\,\mathrm{d}V, \quad SE = \int_S \sigma\,\mathrm{d}S \\ \text{and} \quad W = \int_t \int_V \frac{\eta}{2}\,\|\dot{\boldsymbol{\gamma}}\|^2\,\mathrm{d}V\,\mathrm{d}t, \end{aligned}\right\} \tag{3.1a–d}$$

where V is the drop volume, and S is the drop surface. The drop's viscous dissipation is split into the axial contribution

$$W_b = \int_t \int_V \frac{\eta}{2}\left(\frac{\dot{\gamma}_{xx}^2 + \dot{\gamma}_{yy}^2 + \dot{\gamma}_{zz}^2}{2}\right)\mathrm{d}V\,\mathrm{d}t \tag{3.2}$$

https://doi.org/10.1017/jfm.2024.1164 Published online by Cambridge University Press

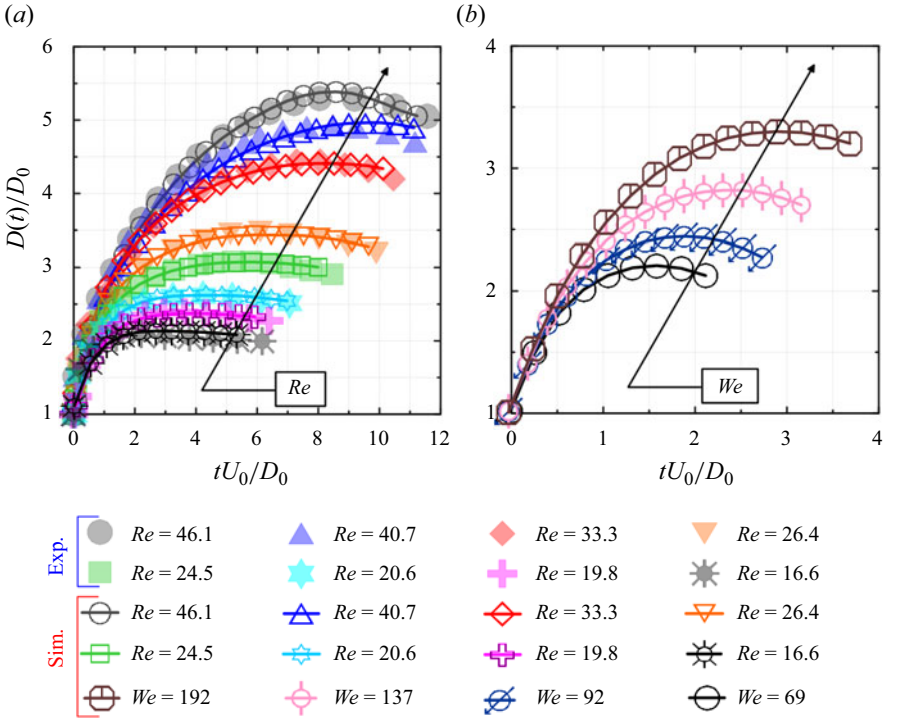


Figure 5. Instantaneous dimensionless diameter $D(t)/D_0$ as a function of the dimensionless time tU_0/D_0. (*a*) Reynolds effects on $D(t)/D_0$. Experiments are represented by the solid symbols, while the numerical simulations are shown with the open ones. Each curve is related to a specific Re in the range 16.6–46.1 at $We = 3432$. (*b*) Weber number effects on $D(t)/D_0$ are numerically stressed at $Re = 161.5$ for $69 \leqslant We \leqslant 192$ (each curve being associated with a particular We).

(where $\dot{\gamma}_{xx} = 2\,\partial u_x/\partial x$, $\dot{\gamma}_{yy} = 2\,\partial u_y/\partial y$ and $\dot{\gamma}_{zz} = 2\,\partial u_z/\partial z$) and its complementary shear-based part $W_c = W - W_b$. These energy terms are plotted together with the viscous dissipation within the vapour film. The latter is defined as

$$W_v = \int_t \int_{V_v} \frac{\eta_v}{2} \|\dot{\boldsymbol{\gamma}}\|^2 \,\mathrm{d}V_v \,\mathrm{d}t, \tag{3.3}$$

in which V_v is the instantaneous volume of the vapour film located between the spreading drop and bottom wall of the computational box. (Both the kinetic energy and the gravitational energy associated with the vapour film are negligible, lower than 5 % of the initial kinetic energy of the drop largely because of the very low vapour density, and thus not shown for clarity.) Each energy term is made dimensionless by the initial energy of the system $E_0 = KE(t = t_0) + SE(t = t_0) + G(t = t_0)$: $G^* = G/E_0$ (green squares), $KE^* = KE/E_0$ (blue triangles), $SE^* = SE/E_0$ (grey circles), $W^* = W/E_0$ (red diamonds), $W_b^* = W_b/E_0$ (magenta crosses), $W_c^* = W_c/E_0$ (black asterisks) and $W_v^* = W_v/E_0$ (inverted orange triangles). In addition, each plot is related to a specific $Re - We$ couple: $Re = 1700$ and $We = 72.25$ in figure 6(*a*), $Re = 170$ and $We = 72.25$ in figure 6(*b*), $Re = 17$ and $We = 72.25$ in figure 6(*c*), $Re = 17$ and $We = 722.5$ in figure 6(*d*), $Re = 17$ and $We = 7225$ in figure 6(*e*), and $Re = 17$ and $We = 72\,250$ in figure 6(*f*). The dashed vertical lines indicate the dimensionless instant at which D_{max} is achieved (e.g. $t_{max}U_0/D_0$); consequently, the grey zone is related to the drop retraction movement.

https://doi.org/10.1017/jfm.2024.1164 Published online by Cambridge University Press

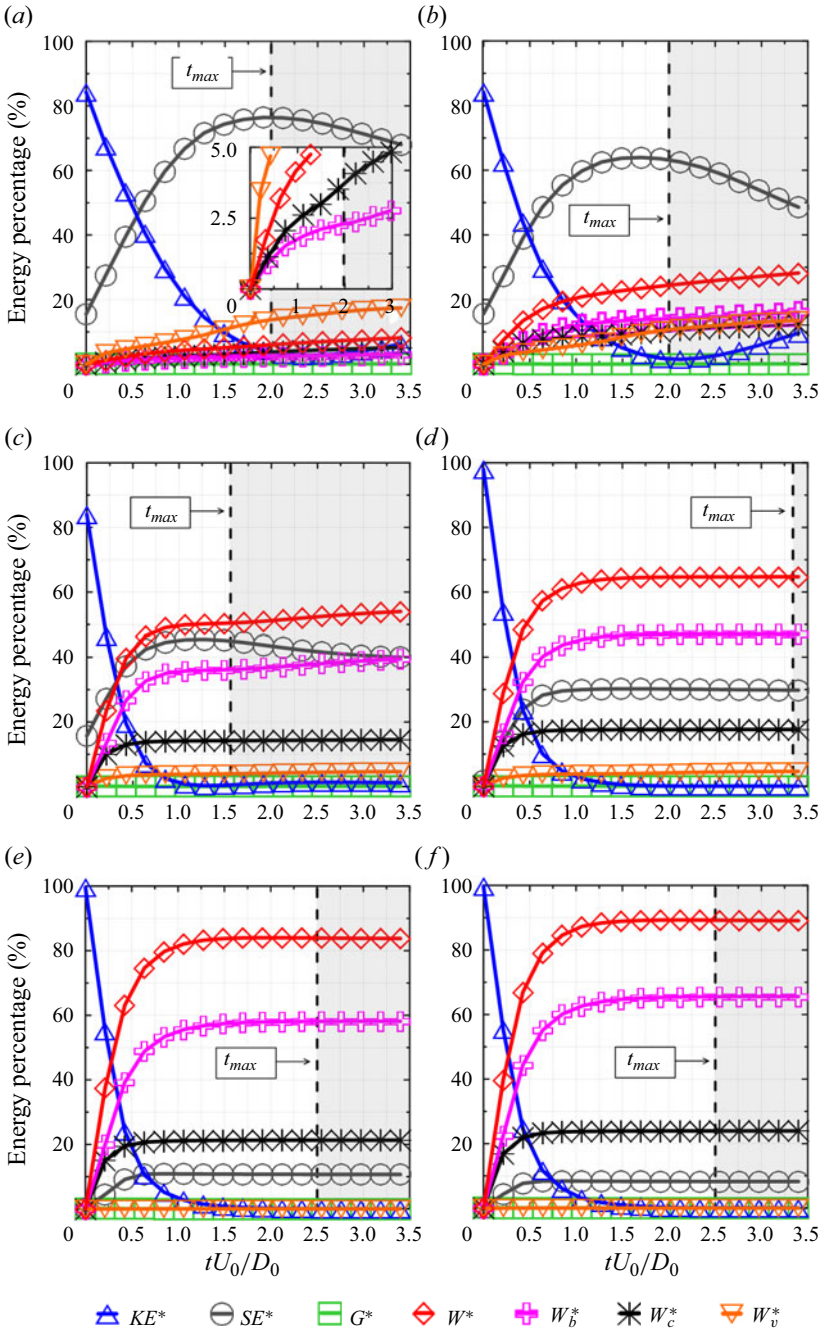


Figure 6. Energy percentage curves plotted as a function of tU_0/D_0 for levitating drops: gravitational energy G^* (green squares), kinetic energy KE^* (blue triangles), surface energy SE^* (grey circles) and dissipation W^* (red diamonds). The latter is split into an axial contribution W_b^* (magenta crosses) and its complementary part $W_c^* = W^* - W_b^*$ (black asterisks). The viscous dissipation within the vapour film W_v^* is also shown (inverted orange triangles). Data are shown at six $Re - We$ couples: (*a*) $Re = 1700$ and $We = 72.25$; (*b*) $Re = 170$ and $We = 72.25$; (*c*) $Re = 17$ and $We = 72.25$; (*d*) $Re = 17$ and $We = 722.5$; (*e*) $Re = 17$ and $We = 7225$; (*f*) $Re = 17$ and $We = 72\,250$. The dashed vertical lines in each plot indicate the dimensionless instant at which D_{max} is achieved (e.g. $t_{max}U_0/D_0$); consequently, the grey zone is related to the drop retraction movement.

https://doi.org/10.1017/jfm.2024.1164 Published online by Cambridge University Press

For all cases shown in figure 6, the spreading is basically induced by the initial kinetic energy of the drop ($KE^*(t = t_0) \geqslant 80\,\%$), which is converted into surface energy and dissipated by viscous effects. At $Re = 1700$ and $We = 72.25$ (figure 6*a*), KE^* is converted primarily into SE^*, indicating that the expansion dynamics is dominated by the balance between inertial and capillary stresses. This is an inertio-capillary regime. As Re decreases at a fixed We, dissipation becomes more pronounced (figure 6*b*), eventually dominating the spreading (figures 6*c*,*d*). Logically, as observed by comparing figures 6(*d*)–6(*f*), dissipation is also strengthened when increasing We at a fixed Re. In such a scenario, the drop expansion is driven by a competition between inertial and viscous stresses. This is an inertio-viscous regime. Furthermore, the dissipation mechanism is associated primarily with biaxial extensional deformations, as underlined by W_b^* (magenta crosses) and W_c^* (black asterisks) in figures 6(*d*)–6(*f*), i.e. $W_b^* > W_c^*$.

It is important to emphasize that although W^* is much lower than SE^* in the inertio-capillary regime (figures 6*a*,*b*), the former exhibits equivalent axial and shear components ($W_b^* \approx W_c^*$). Note that in figure 6(*a*), W_c^* is even slightly higher than W_b^*, as highlighted by the inset plot. Hence in the inertio-capillary regime, levitating drops undergo a complex flow combining biaxial extension with non-negligible shear. The shear component's strengthening is induced by the interactions between the drop and the vapour film, whose viscous dissipation (inverted orange triangles) is comparable to the dissipation within the drop (red diamonds). Nevertheless, as we move from the inertio-capillary regime towards the inertio-viscous regime, SE^* gradually decreases, while W^* increases, eventually becoming higher than W_v^*. As a result, W_b^* overtakes W_c^* and finally dominates the dissipative mechanism in the inertio-viscous regime.

For comparison purposes, we also perform free-slip-based 3-D numerical simulations. After the normal impact, the drop expands freely along the radial direction while its normal velocity remains equal to zero at the free-slip bottom wall (no inlet vapour velocity, $u_{v,z} = 0$ m s^{-1}, no vapour film, and therefore no drop levitation). Energy percentage curves related to six of these simulations are illustrated in figure 7. Their corresponding $Re - We$ couples are similar to those shown in figure 6. Once again, both inertio-capillary and inertio-viscous regimes are observed, depending on Re and We. However, since the vapour film initially located below the drop naturally vanishes after the impact because of the free-slip boundary conditions, W_v^* is sent to zero. Consequently, W_b^* surpasses W_c^* for all the illustrated cases ($W_b^* > W_c^*$).

Comparisons between figures 6 and 7 allow us to conclude that the absence of vapour film resulting from a free-slip scenario favours the development of a dominant biaxial extensional flow in the drop, regardless of the impact regime. On the contrary, the presence of the vapour film induces a shear flow accentuation within levitating drops, which becomes preponderant particularly in the inertio-capillary regime (figure 6*a*). Nevertheless, contrasts between levitating and free-slip drops tend to be mitigated when considering inertio-viscous impact events, as observed by confronting figures 6(*f*) and 7(*f*). The influence of these differences and similarities on D_{max} is underlined in the next subsection.

Interestingly, no Reynolds number effect on $t_{max}U_0/D_0$ is observed when moving from figure 6(*a*) to figure 6(*b*), or from figure 7(*a*) to figure 7(*b*). In other words, in the inertio-capillary regime, $t_{max}U_0/D_0$ is insensitive to variations of the drop viscous dissipation level. In the same way, no Weber number effect on $t_{max}U_0/D_0$ is detected in the inertio-viscous regime, as pointed out by comparing either figures 6(*e*) and 6(*f*), or figures 7(*e*) and 7(*f*). Nevertheless, both Re and We play a relevant

https://doi.org/10.1017/jfm.2024.1164 Published online by Cambridge University Press

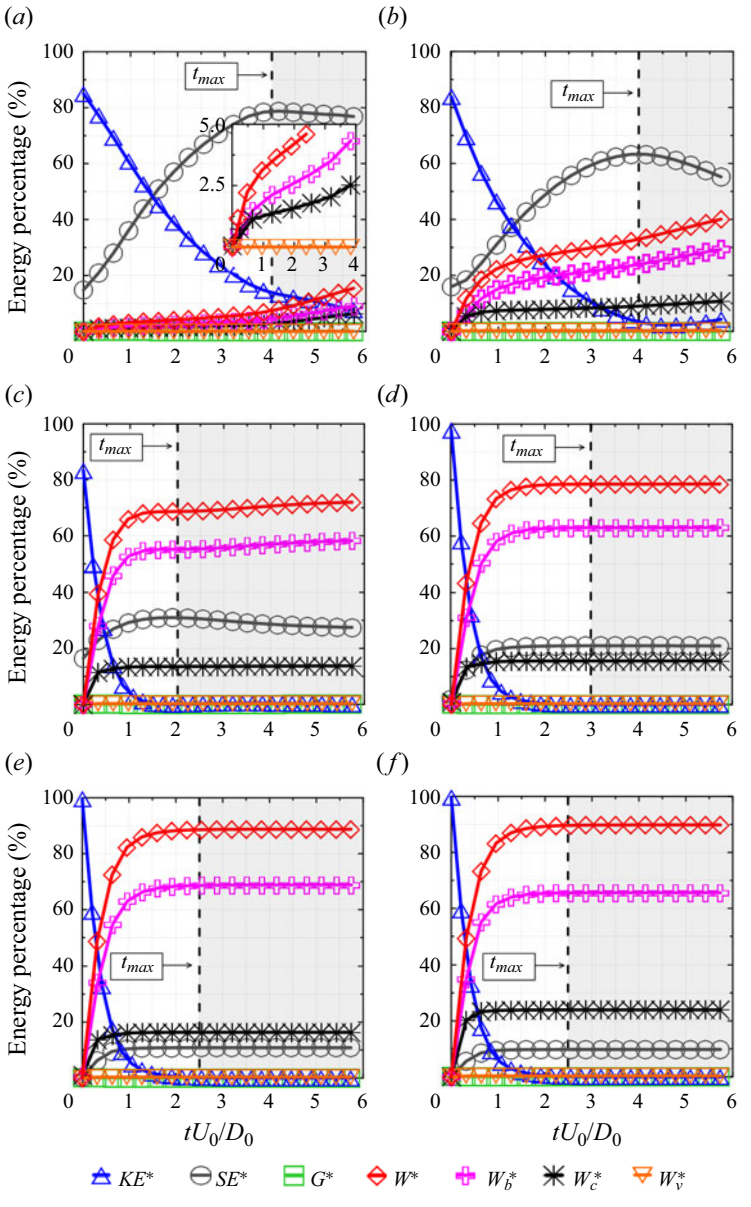


Figure 7. Same plots as in figure 6 using free-slip drops: (*a*) $Re = 1700$, $We = 72.25$; (*b*) $Re = 170$, $We = 72.25$; (*c*) $Re = 17$, $We = 72.25$; (*d*) $Re = 17$, $We = 722.5$; (*e*) $Re = 17$, $We = 7225$; (*f*) $Re = 17$, $We = 72\,250$.

role when transitioning between the mentioned spreading regimes, as observed by confronting figures 6(*b*)–6(*d*), or figures 7(*b*)–7(*d*). This point will be depicted in the next subsection.

Finally, it is important to highlight that, as anticipated in § 2 and confirmed by figures 6 and 7, the use of millimetric drops leads to negligible gravitational effects ($G^*(t) < 5\,\%$, green squares).

https://doi.org/10.1017/jfm.2024.1164 Published online by Cambridge University Press

3.3. *Scaling laws: the drop's maximum spreading and spreading time*

Based on the energy transfer analyses conducted above, we propose scaling laws for D_{max} and t_{max} by considering two spreading regimes: the inertio-capillary regime (figures 6*a*,*b* and 7*a*,*b*) and the inertio-viscous regime (figures 6*d*–*f* and 7*d*–*f*).

In the inertio-capillary spreading regime, the impacting kinetic energy ($\sim\rho U_0^2 D_0^3$) is converted primarily into surface energy at t_{max} ($\sim\sigma D_{max}^2$), leading to

$$\frac{D_{max}}{D_0} \sim \sqrt{We} \quad \text{(inertio-capillary regime)}, \tag{3.4}$$

a well-known scaling law discussed extensively in previous works (Clanet *et al.* 2004; Eggers *et al.* 2010; Laan *et al.* 2014; Josserand & Thoroddsen 2016). On the other hand, in the inertio-viscous regime, the initial kinetic energy is dissipated mainly by viscous effects through a biaxial extension. (Here, $\sim\eta(U_0/D_{max})D_{max}^3$, where D_{max} is taken as the characteristic biaxial-extension-based dissipative length, and U_0/D_{max} represents the characteristic deformation rate in a biaxial extensional spreading, as illustrated by figure 4(*d*), where $\|\dot{\boldsymbol{\gamma}}\|$ clearly appears as a decreasing function of the drop diameter and disconnected from the z direction; this term can be interpreted as an estimation of the work related to the viscous force, i.e. the product of the viscous force $\sim\eta(U_0/D_{max})D_{max}^2$ to the displacement associated with the drop expansion $\sim D_{max}$.) Hence we find

$$\frac{D_{max}}{D_0} \sim \sqrt{Re} \quad \text{(inertio-viscous regime)}, \tag{3.5}$$

which, to our best knowledge, is proposed for the first time. The inertio-viscous scaling associated with the biaxial extensional dissipative process differs from the classical $D_{max}/D_0 \sim Re^{1/5}$ one, which in turn emerges from a shear-based dissipative mechanism whose characteristic length is $\sim H_{min}$ and characteristic deformation rate is $\sim U_0/H_{min}$ (with $H_{min} \sim D_0^3/D_{max}^2$ by mass conservation; see more detail in Clanet *et al.* 2004; Fedorchenko, Wang & Wang 2005; Eggers *et al.* 2010; Laan *et al.* 2014; Isukwem *et al.* 2024*b*). By equating our scaling laws (3.4) and (3.5), we find $\sqrt{We/Re} \sim 1$. This equation contains a dimensionless parameter called here the impact number. It is, by coincidence, equal to the square root of the capillary number Ca (which is defined as $Ca = We/Re = \eta U_0/\sigma$). It tends to 1 when transitioning from the inertio-capillary spreading regime to the inertio-viscous one.

The validity of the above theoretical arguments is corroborated by figure 8(*a*), in which the rescaled maximum spreading $D_{max}/D_0/\sqrt{Re}$ is plotted as a function of $\sqrt{We/Re}$ not only for experimental results (solid triangles and diamonds), but also for the numerical levitating drops (open circles). The results collapse across a single path divided into three regions highlighting different spreading regimes: inertio-capillary (I, blue box), for which $D_{max}/D_0 \sim \sqrt{We}$; inertio-viscous (II, red box), where $D_{max}/D_0 \sim \sqrt{Re}$; and a mixed regime (III, white box), for which inertial, capillary and viscous effects all play an essential role. As underlined by our theoretical analyses, a mixed regime (transitioning zone) emerges when $2 < \sqrt{We/Re} < 10$ (e.g. $\sqrt{Ca} \sim 1$). The particular shape of the latter can be understood by the fact that, moving from the left to the right into the transitioning zone, D_{max}/D_0 increases slower than $\sqrt{Re}$ (which, in turn, starts playing an important role; in III, both *We* and *Re* play a relevant role). As a result, $D_{max}/D_0/\sqrt{Re}$ tends to decrease within the mixed inertio-viscous-capillary regime.

For comparison purposes, we also plot in figure 8(*a*) free-slip-based numerical results (green squares). Although the obtained master curve exhibits the same shape as the

https://doi.org/10.1017/jfm.2024.1164 Published online by Cambridge University Press

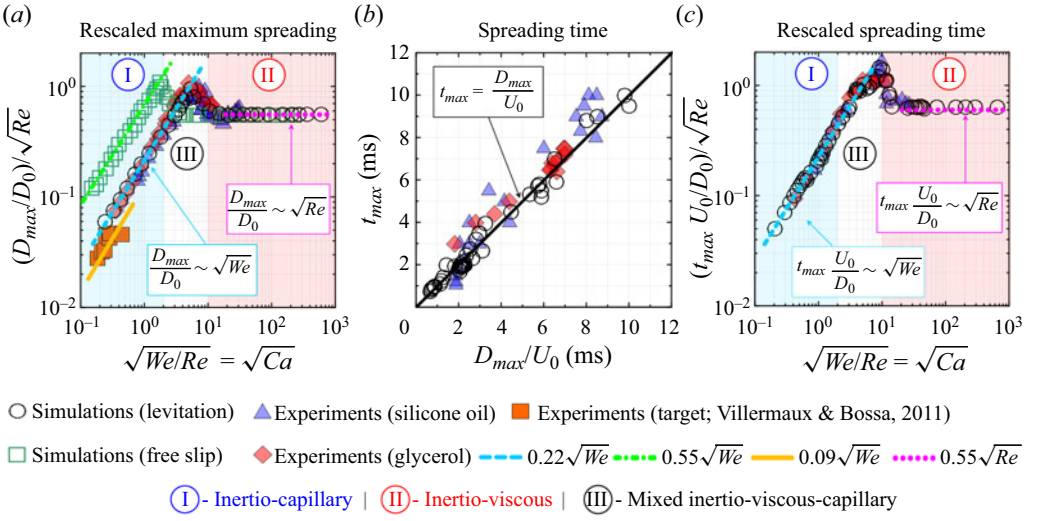


Figure 8. (*a*) Rescaled maximum spreading $(D_{max}/D_0)/\sqrt{Re}$ as a function of the impact number $\sqrt{We/Re}$. (*b*) Spreading time t_{max} as a function of D_{max}/U_0. (*c*) Rescaled spreading time $(t_{max}U_0/D_0)/\sqrt{Re}$ as a function of $\sqrt{We/Re}$. Experimental (solid blue triangles for silicone oils, and solid red diamonds for glycerol solutions) and numerical (grey circles for the inverse Leidenfrost configuration, and green squares for the free-slip-based configuration) results are plotted. They collapse across a single path divided into three regions linked with different spreading regimes: inertio-capillary (I, blue box), for which $D_{max}/D_0 \sim \sqrt{We}$ and $t_{max}U_0/D_0 \sim \sqrt{We}$ (dashed line and dash-dotted line); inertio-viscous (II, red box), where $D_{max}/D_0 \sim \sqrt{Re}$ and $t_{max}U_0/D_0 \sim \sqrt{Re}$ (dotted line); and a mixed regime (III, white box), for which inertial, capillary and viscous effects all play an important role. As underlined by our theoretical analyses, a mixed regime (transitioning zone) emerges when $2 < \sqrt{We/Re} < 10$.

previous one, it is shifted towards the left. Hence at $\sqrt{We/Re} < 2$, a lower spreading level is observed for levitating drops than for free-slip ones. Such a discrepancy emerges from the supplemental viscous dissipation generated by the shear of the vapour film. Note that together with the levitating drop, the vapour film can dissipate approximately 30 % of the initial kinetic energy of the system $(W_v^*(t = t_{max}) + W^*(t = t_{max}) \approx 0.3KE^*(t = t_0)$ in figure 6*a*). This supplemental dissipative source prevents drops from reaching a spreading level similar to that observed in free-slip configurations at $\sqrt{We/Re} < 2$, although the expansion remains essentially driven by a competition between inertial and capillary stresses. Dissipative effects emerging from the vapour film are also perceived through the difference between the prefactors associated with the inverse Leidenfrost inertio-capillary impact regime, $D_{max}/D_0 \approx 0.22\sqrt{We}$ (blue dashed line), and the free-slip inertio-capillary impact regime, $D_{max}/D_0 \approx 0.55\sqrt{We}$ (green dash-dotted line). Interestingly, experimental results related to the maximum expansion of water drops impacting on targets (orange rectangles) reported by Villermaux & Bossa (2011) appear below the inverse-Leidenfrost-based ones, which indicates that the former exhibits a relevant dissipation level as well (this can be associated with viscous shear stresses induced by the target in the centre portion of the drop; more analyses on this topic would be highly welcome).

Finally, the contrast between the free-slip and levitating configurations vanishes in the inertio-viscous regime, for which viscous dissipation is related primarily to biaxial-extensional deformations within the drop. In this regime, $D_{max}/D_0 \approx 0.55\sqrt{Re}$

https://doi.org/10.1017/jfm.2024.1164 Published online by Cambridge University Press

(magenta dotted line). With these differences and similarities being addressed, we focus again on inverse Leidenfrost impacting drops in the following.

By defining the spreading time t_{max} as D_{max}/U_0 (i.e. $t_{max} = D_{max}/U_0$), a result corroborated by figure 8(*b*) where t_{max} is displayed as a function of D_{max}/U_0, we conclude through (3.4) and (3.5) that

$$t_{max}\left(\frac{U_0}{D_0}\right) \sim \sqrt{We} \quad \text{(inertio-capillary regime)} \tag{3.6}$$

and

$$t_{max}\left(\frac{U_0}{D_0}\right) \sim \sqrt{Re} \quad \text{(inertio-viscous regime).} \tag{3.7}$$

The similarity between the above equations and those related to D_{max}/D_0 suggests that the spreading time can be expressed as a function of the impact number. Indeed, by plotting $(t_{max}U_0/D_0)/\sqrt{Re}$ against $\sqrt{We/Re}$ in figure 8(*c*), we observe once again that both the experimental and numerical results collapse across a master curve divided into three regions associated with the inertio-capillary spreading regime (I, blue box, $t_{max}U_0/D_0 \sim \sqrt{We}$), the inertio-viscous spreading regime (II, red box, $t_{max}U_0/D_0 \sim \sqrt{Re}$), and the mixed inertio-viscous-capillary spreading regime (III, white box) for which inertia, capillarity and viscosity are all relevant.

4. Concluding remarks and perspectives

In this paper, we have studied experimentally, numerically and theoretically the normal impact of Newtonian drops in inverse Leidenfrost conditions. More specifically, using a mixed approach combining 3-D numerical simulations and experiments, we have extended previous works on the topic (Arora *et al.* 2018; Louhichi *et al.* 2020; Charles *et al.* 2021), bringing to light the physical mechanism driving the expansion of levitating drops.

We have presented an experimental–numerical–theoretical framework pointing out scaling laws for the drop maximum spreading D_{max} and spreading time t_{max} in different impact regimes in inverse Leidenfrost conditions. This framework can be extended easily to non-Newtonian materials in future studies.

Our results were explored through dynamics analyses, energy transfer and scaling laws, which indicate the existence of three different spreading regimes: (i) inertio-capillary (balancing inertial and capillary stresses in the drop) for which D_{max}/D_0 and $t_{max}U_0/D_0$ scale with $\sqrt{We}$; (ii) inertio-viscous (balancing inertial and viscous stresses in the drop) for which D_{max}/D_0 and $t_{max}U_0/D_0$ scale with $\sqrt{Re}$; and (iii) a mixed regime for which inertia, capillarity and viscosity are all relevant.

Although the inertio-capillary spreading regime is essentially driven by a competition between inertial and capillary stresses in the drop, it is affected by the viscous dissipation emerging from the $O(10^1)$ µm thickness vapour film separating the drop and the solid plate. This non-negligible viscous dissipation not only prevents the drop from achieving a spreading level similar to that observed in free-slip-based numerical simulations, but also favours the development of a shear flow within the impacting object. Nevertheless, these vapour film effects are strongly attenuated by the increase of the impact number ($\sqrt{We/Re} = \sqrt{Ca}$), ultimately becoming marginal in the inertio-viscous spreading regime, whose dissipative mechanism emerges primarily from biaxial deformations.

To our best knowledge, the inertio-viscous scaling law that we have proposed has not been reported so far. It is associated with a biaxial extensional dissipative process

https://doi.org/10.1017/jfm.2024.1164 Published online by Cambridge University Press

whose characteristic deformation rate is $\sim U_0/D_{max}$. Hence it naturally differs from the classical $D_{max}/D_0 \sim Re^{1/5}$ scaling, which in turn emerges from a shear-based dissipative mechanism whose characteristic deformation rate is $\sim U_0/H_{min}$ (Clanet *et al.* 2004; Fedorchenko *et al.* 2005; Eggers *et al.* 2010; Laan *et al.* 2014; Isukwem *et al.* 2024*b*).

Finally, by manipulating the deduced scaling laws, it was shown that the experimental–numerical results obtained here collapse along a single master curve according to which both D_{max} and t_{max} are functions of the impact number.

Our study has direct applications in a number of impact-based situations, which include spray coating, forensic science, firefighting, inkjet printing, atomization, filtration systems, and 3-D printing of organs, tissues, prosthetics and electronic components, among others (Lorenceau & Quéré 2003; Bordoloi & Longmire 2014; Laan *et al.* 2014; Murphy & Atala 2014; Ryu *et al.* 2017; Kumar *et al.* 2018; Soto *et al.* 2018; Vijayavenkataraman *et al.* 2018; Modak *et al.* 2020; Su *et al.* 2020). From a more fundamental standpoint, the impact of drops in Leidenfrost conditions is a non-conventional rheological test that is highly attractive for non-Newtonian materials. It involves flow conditions that are difficult to reach with conventional rheometers, namely large deformations and highly elongational flows on short time scales ($U_0/D_0 \gtrsim O(10^3)$ s^{-1}).

Since complex fluids are frequently used in industrial domains, it would be interesting to consider non-Newtonian effects on the spreading, such as those related to the yield stress and/or elasticity.

Acknowledgements. The authors would like to acknowledge support from the UCA^{JEDI} programme (IDEX of Université Côte d'Azur), the PSL Research University under the programme 'Investissements d'Avenir' launched by the French Government and implemented by the French National Research Agency (ANR) with the reference ANR-10-IDEX-0001-02 PSL.

Funding. Financial support for this work from the ANR under the 'Investissements d'Avenir' program (INNpact project no. ANR-21-CE06-0036), and the H2020 Programme (Marie Curie Actions) of the European Innovative Training Networks (H2020-MSCA-ITN-2017) under DoDyNet REA grant agreement no. 765811, is gratefully acknowledged.

Declaration of interests. The authors report no conflict of interest.

Author ORCIDs.
Christian Ligoure https://orcid.org/0000-0003-3445-6826;
Anselmo Pereira https://orcid.org/0000-0001-6688-1013.

Appendix A

A.1. *Size of the smallest mesh element*

Since we do not measure the minimal thickness of the vapour layer (h_{min}) experimentally, we present in § 2 an estimate calculation (2.5) that leads to values of the same order of magnitude as those reported by Biance *et al.* (2003) and Gauthier *et al.* (2019) under static levitation conditions ($\sim$10 μm). Based on this calculation, we fix the size of the smallest mesh element Δ_{min} as being 10 times smaller h_{min} ($\Delta_{min} = 1$ μm). Hence in the numerical simulations, the drop never touches the bottom part of the computational box (remaining in levitation) if the distance between them is higher than 1 μm, which is the case for all the numerical results reported here ($\Delta_{min} > 1$ μm).

Figure 9 corroborates the arguments below. It illustrates the instantaneous minimal distance between the drop and the bottom wall of the computational box (h_{min}) as a function of time for three different values of Δ_{min} at $Re = 17$ and $We = 72.25$ (typical mixed inertio-viscous-capillary case): 0.1 μm, 1 μm and 10 μm. The yellow box indicates

https://doi.org/10.1017/jfm.2024.1164 Published online by Cambridge University Press

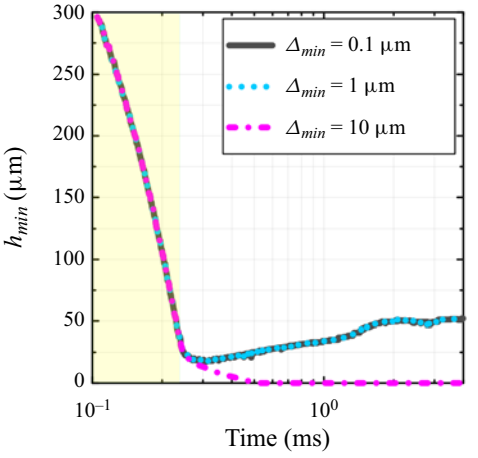


Figure 9. Instantaneous minimal distance between the drop and the bottom wall of the computational box (h_{min}) as a function of time for three different values of Δ_{min} at $Re = 17$ and $We = 72.25$ (typical mixed inertio-viscous-capillary case): 0.1 μm (grey solid line), 1 μm (blue dotted line) and 10 μm (magenta dash-dotted line). The yellow box indicates the initial drop fall (no expansion), which is followed by the drop expansion indicated by the white box.

the initial drop fall (no expansion), which is followed by the drop expansion indicated by the white box. As observed, similar h_{min} curves are obtained at $\Delta_{min} = 0.1$ μm and $\Delta_{min} = 1$ μm (similar diameter and energy transfer curves are equally obtained; not shown, for brevity). However, the vapour layer is not able to maintain the drop in levitation when $\Delta_{min} = 10$ μm. These results give us confidence to fix Δ_{min} at 1 μm.

A.2. *Interface capturing*

The level-set method, introduced by Osher & Sethian (1988), has been applied to numerous two-fluid flows. It consists first in computing the signed distance function to the interface α. As shown in figure 10(a), which describes its initial value, this function is positive in Ω_f and negative in Ω_{vapour}, where Ω denotes the computational fluid domain ($\Omega \subset \mathbb{R}^n$, at time $t \in [0, T]$). The zero value corresponds to the interface between the two sub-domains:

$$\alpha(\boldsymbol{x}) = \begin{cases} d(\boldsymbol{x}, \Gamma), & \boldsymbol{x} \in \Omega_f, \\ -d(\boldsymbol{x}, \Gamma), & \boldsymbol{x} \in \Omega_{vapour}, \\ 0, & \boldsymbol{x} \in \Gamma. \end{cases} \tag{A1}$$

Then we need to follow the interface during the simulation. Thus the transport equation of the level-set function should be solved, giving the new interface location:

$$\begin{cases} \dfrac{\partial \alpha}{\partial t} + \boldsymbol{v} \cdot \nabla \alpha = 0, \\ \alpha(t = 0, \boldsymbol{x}) = \alpha_0(\boldsymbol{x}). \end{cases} \tag{A2}$$

This method is often applied in phase transformation and multiphase flows (Osher & Fedkiw 2001; Ji, Chopp & Dolbow 2002). Indeed, it allows us to describe a wide range of problems, as it can handle problems where the surface evolves in fairly complex ways with high topology changes. Then intrinsic geometric properties of the interface, such as normal

https://doi.org/10.1017/jfm.2024.1164 Published online by Cambridge University Press

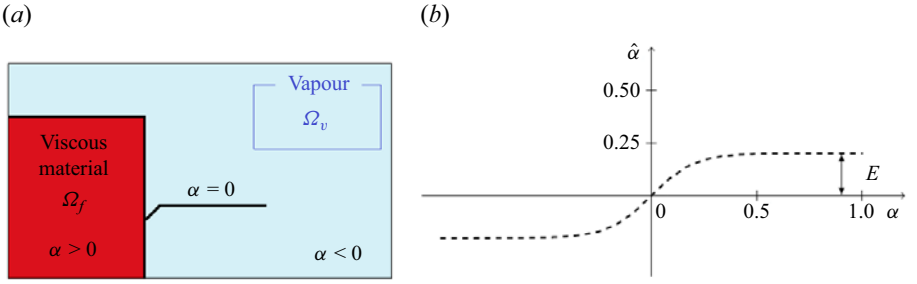


Figure 10. (*a*) Viscous phase (red) surrounded by a vapour phase (blue). (*b*) Filtering curve for the level-set function.

vectors or curvatures, are determined from the level-set field. However, some additional treatments, listed below, are necessary to improve the efficiency of this approach.

A.3. *Redistancing and filtering of the level-set function*

After the resolution of the transport equation (A2), many oscillations may appear close to the interface, polluting the interface quality. Indeed, the isocontours of the level-set function are no longer smooth, leading to the loss of its metric property $\|\nabla\alpha\| = 1$. Thus a reinitialization step is performed by solving the Hamilton–Jacobi equation to ensure $\|\nabla\alpha\| = 1$.

Moreover, during the convection of the level-set function, high gradient changes may occur, giving rise to instabilities and then polluting the final solution. Usually, a filtering function $\hat{\alpha}$ is defined, equal to zero at the interface, approaching α close to the interface, and keeping constant value far from the interface. Several filtering functions can be found in the literature (Olsson & Kreiss 2005; Bonito, Guermond & Lee 2015; Khalloufi *et al.* 2016). In this work, a hyperbolic tangential filter is used. Thus the new filtered level-set function $\hat{\alpha}$ is computed as

$$\hat{\alpha} = E \times \tanh\left(\frac{\alpha}{E}\right), \tag{A3}$$

where E corresponds to the interface thickness; figure 10(*b*) shows a typical plot of $\hat{\alpha}$, which tends to E as α increases.

Thus the reinitialization equations can be updated, taking into account the filtered level-set function $\hat{\alpha}$. The gradient of $\hat{\alpha}$ is computed as

$$\frac{\partial\hat{\alpha}(\alpha)}{\partial\alpha} = 1 - \tanh^2\left(\frac{\alpha}{E}\right), \tag{A4}$$

and is formulated with respect to $\hat{\alpha}$ as

$$\frac{\partial\hat{\alpha}(\alpha)}{\partial\alpha} = 1 - \left(\frac{\hat{\alpha}(\alpha)}{E}\right)^2. \tag{A5}$$

Then a new fictive step, called t_f, is introduced. The purpose consists in finding a new parametric function β where the reinitialization step must be performed, and having the

https://doi.org/10.1017/jfm.2024.1164 Published online by Cambridge University Press

same isovalue α such that

$$\|\nabla\beta\| = 1. \tag{A6}$$

The Hamilton–Jacobi equation is then formulated as

$$\begin{cases} \dfrac{\partial\beta}{\partial t_f} + s(\beta)(\|\nabla\beta\| - 1) = 0, \\ \beta(t_f = 0, \boldsymbol{x}) = \alpha(t, \boldsymbol{x}). \end{cases} \tag{A7}$$

Considering now the filtering level-set function $\hat{\alpha}$, the Hamilton–Jacobi equation becomes

$$\begin{cases} \dfrac{\partial\beta}{\partial t_f} + s(\hat{\alpha})\left[\|\nabla\hat{\alpha}\| - \left(1 - \left(\dfrac{\hat{\alpha}}{E}\right)^2\right)\right] = 0, \\ \beta(t_f = 0, \boldsymbol{x}) = \alpha(t, \boldsymbol{x}). \end{cases} \tag{A8}$$

By turning (A8) into a transport equation, the problem is rewritten as

$$\begin{cases} \dfrac{\partial\beta}{\partial t_f} + \boldsymbol{U}\cdot\nabla\hat{\alpha} = s(\hat{\alpha})\left[1 - \left(\dfrac{\hat{\alpha}}{E}\right)^2\right], \\ \beta(t_f = 0, \boldsymbol{x}) = \alpha(t, \boldsymbol{x}), \end{cases} \tag{A9}$$

with

$$\boldsymbol{U} = \frac{s(\hat{\alpha})\,\nabla\hat{\alpha}}{\|\nabla\hat{\alpha}\|}. \tag{A10}$$

A.4. *Coupling transport and redistancing steps*

We couple both the transport and the Hamilton–Jacobi equations (Khalloufi *et al.* 2016). This step reduces the system to finally one global transport equation, and will consequently eliminate the frequency parameter for the reinitialization. Thus we define λ as the ratio between fictive and real time steps:

$$\lambda = \frac{\partial t_f}{\partial t}. \tag{A11}$$

Then, by choosing λ such that $\lambda = l/\triangle t$, where l is the mesh size, one obtains

$$\frac{\partial\beta}{\partial t} = \lambda\frac{\partial\beta}{\partial t_f}. \tag{A12}$$

Introducing (A12) in (A9), the new convection-reinitialization equation is obtained:

$$\frac{\partial\beta}{\partial t} + \lambda\boldsymbol{U}\cdot\nabla\hat{\alpha} = \lambda\, s(\hat{\alpha})\left[1 - \left(\frac{\hat{\alpha}}{E}\right)^2\right]. \tag{A13}$$

Therefore, in particular at the interface, the equation that couples the transport and the reinitialization steps will be formulated as

$$\frac{\partial\hat{\alpha}}{\partial t} + (\boldsymbol{u} + \lambda\boldsymbol{U})\cdot\nabla\hat{\alpha} = \lambda\, s(\hat{\alpha})\left[1 - \left(\frac{\hat{\alpha}}{E}\right)^2\right]. \tag{A14}$$

https://doi.org/10.1017/jfm.2024.1164 Published online by Cambridge University Press

This new equation leads to the appearance of a new convection term: $(\boldsymbol{u} + \lambda \boldsymbol{U}) \cdot \boldsymbol{\nabla} \hat{\alpha}$. The associated variational formulation is: find $\hat{\alpha} \in \mathcal{L}^2(\Omega)$ such that

$$\left(\frac{\partial \hat{\alpha}}{\partial t}, \Phi_v\right)_{\Omega} + \left[(\boldsymbol{u} + \lambda \boldsymbol{U}) \cdot \boldsymbol{\nabla} \hat{\alpha}, \Phi_v\right]_{\Omega} = \left[\lambda s(\hat{\alpha}) \left(1 - \left(\frac{\hat{\alpha}}{E}\right)^2\right), \Phi_v\right]_{\Omega} \tag{A15}$$

for all $\Phi_v \in \mathcal{L}^2(\Omega)$.

The problem is then discretized with respect to time by using a second-order backward differentiation (BFD2) method. Finally, the discretized problem is

$$\begin{aligned} &\left(\frac{3\hat{\alpha}^{n+1} - 4\hat{\alpha}^n + \hat{\alpha}^{n-1}}{2\,\Delta t}, \Phi_v\right)_{\Omega} + \left[(\boldsymbol{u} + \lambda \boldsymbol{U}) \cdot \boldsymbol{\nabla} \hat{\alpha}^{n+1}, \Phi_v\right]_{\Omega} \\ &\quad = \left[\lambda s(\hat{\alpha}^n) \left(1 - \left(\frac{\hat{\alpha}^n}{E}\right)^2\right), \Phi_v\right]_{\Omega}. \end{aligned} \tag{A16}$$

A.5. *Method of resolution – momentum and mass equations*

The numerical simulation of viscoplastic flows leads to the resolution of momentum and mass equations (analogue to the incompressible Navier–Stokes equations for Newtonian fluids). The computational fluid domain is defined such that $\Omega \subset \mathbb{R}^n$ at time $t \in [0, T]$. This problem consists in finding velocity and pressure fields (u and p), defined respectively in the spaces $V = \mathbb{R}^n$, $P = \mathbb{R}$, such that

$$\begin{cases} \rho \left(\dfrac{\partial \boldsymbol{u}}{\partial t} + \boldsymbol{u} \cdot \boldsymbol{\nabla} \boldsymbol{u}\right) + \boldsymbol{\nabla} p - \boldsymbol{\nabla} \cdot \boldsymbol{\tau} = \boldsymbol{f}, \\ \boldsymbol{\nabla} \cdot \boldsymbol{u} = 0, \end{cases} \tag{A17}$$

where $\boldsymbol{\tau}$ and $\boldsymbol{f}$ correspond respectively to the extra-stress tensor and the source term (here, $\boldsymbol{f} = \boldsymbol{f}_{st}$). Recall that the viscous fluid and vapour densities (ρ_f and ρ_{vapour}) and viscosities (η_f and η_{vapour}) are mixed (into ρ and η, respectively) and computed using the Heaviside function of the filtered level-set $H(\hat{\alpha})$.

References

Adda-Bedia, M., Kumar, S., Lechenault, F., Moulinet, S., Schillaci, M. & Vella, D. 2016 Inverse Leidenfrost effect: levitating drops on liquid nitrogen. *Langmuir* **17**, 4179–4188.

Arora, S., Fromental, J.-M., Mora, S., Phou, T., Ramos, L. & Ligoure, C. 2018 Impact of beads and drops on a repellent solid surface: a unified description. *Phys. Rev. Lett.* **120**, 148003.

Arora, S., Ligoure, C. & Ramos, L. 2016 Interplay between viscosity and elasticity in freely expanding liquid sheets. *Phys. Rev. Fluids* **1**, 083302.

Arora, S., Louhichi, A., Vlassopoulos, D., Ligoure, C. & Ramos, L. 2021 Instabilities in freely expanding sheets of associating viscoelastic fluids. *Soft Matt.* **17**, 10935–10945.

Biance, A.-L., Clanet, C. & Quéré, D. 2003 Leidenfrost drops. *Phys. Fluids* **15**, 1632–1637.

Blackwell, B.C., Deetjen, M.E., Gaudio, J.E. & Ewoldt, R.H. 2015 Sticking and splashing in yield-stress fluid drop impacts on coated surfaces. *Phys. Fluids* **27**, 043101.

Bonito, A., Guermond, J.-L. & Lee, S. 2015 Numerical simulations of bouncing jets. *Intl J. Numer. Meth. Fluids* **80**, 53–75.

Bonn, D., Eggers, J., Indekeu, J., Meunier, J. & Rolley, E. 2009 Wetting and spreading. *Rev. Mod. Phys.* **81**, 739.

Bordoloi, A.D. & Longmire, E.K. 2014 Drop motion through a confining orifice. *J. Fluid Mech.* **759**, 520–545.

https://doi.org/10.1017/jfm.2024.1164 Published online by Cambridge University Press

BOYER, F., SANDOVAL-NAVA, E., SNOEIJER, J.H., DIJKSMAN, J.F. & LOHSE, D. 2016 Drop impact of shear thickening liquids. *Phys. Rev. Fluids* **1**, 013901.

CARLSON, A., DO-QUANG, M. & AMBERG, G. 2011 Dissipation in rapid dynamic wetting. *J. Fluid Mech.* **682**, 213–240.

CHARLES, C.-A., LOUHICHI, A., RAMOS, L. & LIGOURE, C. 2021 Viscoelasticity and elastocapillarity effects in the impact of drops on a repellent surface. *Soft Matt.* **17**, 5829–5837.

CLANET, C., BÉGUIN, C., RHICHARD, D. & QUÉRÉ, D. 2004 Maximal deformation of an impacting drop. *J. Fluid Mech.* **517**, 199–208.

COMTET, J., KESHAVARZ, B. & BUSH, J.W.M. 2016 Drop impact and capture on a thin flexible fiber. *Soft Matt.* **12**, 149–156.

COOPER-WHITE, J.J., CROOKS, R.C. & BOGER, D.V. 2002 A drop impact study of worm-like viscoelastic surfactant solutions. *Colloids Surf. (*A*)* **210**, 105–123.

COUPEZ, T. & HACHEM, E. 2013 Solution of high-Reynolds incompressible flow with stabilized finite element and adaptive anisotropic meshing. *Comput. Meth. Appl. Mech. Engng* **267**, 65–85.

CROOKS, R.C. & BOGER, D.V. 2000 Influence of fluid elasticity on drops impacting on dry surfaces. *J. Rheol.* **44**, 973–996.

DUEZ, C., YBERT, C., CLANET, C. & BOCQUET, L. 2010 Wetting controls separation of inertial flows from solid surfaces. *Phys. Rev. Lett.* **104**, 084503.

EGGERS, J., FONTELOS, M.A., JOSSERAND, C. & ZALESKI, S. 2010 Drop impact after impact on a solid wall: theory and simulations. *Phys. Fluids* **22**, 062101.

FEDORCHENKO, A.I., WANG, A.-B. & WANG, Y.-H. 2005 Effect of capillary and viscous forces on spreading of a liquid drop impinging on a solid surface. *Phys. Fluids* **17**, 093104.

GARMETT, W. 1878 Leidenfrost' phenomenon. *Nature* **17**, 466.

GAUTHIER, A., DIDDENS, C., PROVILLE, R., LOHSE, D. & VAN DER MEER, D. 2019 Self-propulsion of inverse Leidenfrost drops on a cryogenic bath. *Proc. Natl Acad. Sci. USA* **116**, 1174–1179.

GRAEBER, G., REGULAGADDA, K., HODEL, P., KUTTEL, C., LANDOLF, D., SCHUTZIUS, T.M. & POULIKAKOS, D. 2021 Leidenfrost droplet trampolining. *Nat. Commun.* **12**, 1–7.

GUO, Y. & LIAN, Y. 2018 Numerical investigation of oblique impact of multiple drops on thin liquid film. *J. Colloid Interface Sci.* **530**, 586–594.

HACHEM, E., KHALLOUFI, M., BRUCHON, J., VALETTE, R. & MESRI, Y. 2016 Unified adaptive variational multiscale method for two phase compressible and incompressible flows. *Comput. Meth. Appl. Mech. Engng* **308**, 238–255.

HALL, R.S., BOARD, S.J., CLARE, A.J., DUFFEY, R.B., PLAYLE, T.S. & POOLE, D.H. 1969 Inverse Leidenfrost phenomenon. *Nature* **224**, 266–267.

ISUKWEM, K., GODEFROID, G., MONTEUX, C., BOUTTES, D., CASTELLANI, R., HACHEM, E., VALETTE, R. & PEREIRA, A. 2024*b* The role of viscoplastic drop shape in impact. *J. Fluid Mech.* **978**, A1.

ISUKWEM, K., HACHEM, E. & PEREIRA, A. 2024*a* Etude théorique et numérique sur l'étalement d'objects viscoplastiques bidimensionnels impactant une surface solide. *Rhélogie* **45**, 35–43.

ISUKWEM, K., NEMER, R., HACHEM, E. & PEREIRA, A. 2024*c* Viscoplastic elliptical objects impacting a solid surface. *Phys. Fluids* **36**, 033125.

JI, H., CHOPP, D. & DOLBOW, J.E. 2002 A hybrid extended finite element/level set method for modeling phase transformations. *Intl J. Numer. Meth. Engng* **54**, 1209–1233.

JOSSERAND, C. & THORODDSEN, S.T. 2016 Drop impact of yield-stress fluids. *Annu. Rev. Fluid Mech.* **48**, 365–391.

KHALLOUFI, M., MESRI, Y., VALETTE, R., MASSONI, E. & HACHEM, E. 2016 High fidelity anisotropic adaptive variational multiscale method for multiphase flows with surface tension. *Comput. Meth. Appl. Mech. Engng* **307**, 44–67.

KUMAR, A., TRIPATHY, A., NAM, Y., LEE, C. & SEN, P. 2018 Effect of geometrical parameters on rebound of impacting droplets on leaky superhydrophobic meshes. *Soft Matt.* **14**, 1571–1580.

LAAN, N., DE BRUIN, K.G., BARTOLO, D., JOSSERAND, C. & BONN, D. 2014 Maximum diameter of impacting liquid droplets. *Phys. Rev. Appl.* **2**, 044018.

LECLEAR, S., LECLEAR, J., ABHIJEET, PARK, K.-C. & CHOI, W. 2016 Drop impact on inclined superhydrophobic surfaces. *J. Colloid Interface Sci.* **461**, 114–121.

LEE, J.B., LAAN, N., DE BRUIN, K.G., SKANTZARIS, G., SHAHIDZADEH, N., DEROME, D., CARMELIET, J. & BONN, D. 2015 Universal rescaling of drop impact on smooth and rough surfaces. *J. Fluid Mech.* **786**, R4.

LEE, S.-H., HARTH, K., RUMP, M., KIM, M., LOHSE, D., FEZZAA, K. & JE, J.H. 2020 Drop impact on hot plates: contact times, lift-off and the lamella rupture. *Soft Matt.* **16**, 7935–7949.

https://doi.org/10.1017/jfm.2024.1164 Published online by Cambridge University Press

LEIDENFROST, J.G. 1756 De aquae communis nonnullis qualitatibus tractatus. Ovenius, Duisburg, Germany.
LORENCEAU, E., CLANET, C. & QUÉRÉ, D. 2004 Capturing drops with a thin fiber. *J. Colloid Interface Sci.* **279**, 192–197.
LORENCEAU, E. & QUÉRÉ, D. 2003 Drops impacting a sieve. *J. Colloid Interface Sci.* **263**, 244–249.
LOUHICHI, A., CHARLES, C.-A., PHOU, T., VLASSOPOULOS, D., RAMOS, L. & LIGOURE, C. 2020 Biaxial extensional viscous dissipation in sheets expansion formed by impact of drops of Newtonian and non-Newtonian fluids. *Phys. Rev. Fluids* **5**, 053602.
LUU, L.-H. & FORTERRE, Y. 2009 Drop impact of yield-stress fluids. *J. Fluid Mech.* **632**, 301–327.
LUU, L.-H. & FORTERRE, Y. 2014 Giant drag reduction in complex fluid drops on rough hydrophobic surfaces. *Phys. Rev. Lett.* **110**, 184501.
MODAK, C.D., KUMAR, A., TRIPATHY, A. & SEN, P. 2020 Drop impact printing. *Nat. Commun.* **11**, 1–11.
MURPHY, S.V. & ATALA, A. 2014 3D bioprinting of tissues and organs. *Nat. Biotechnol.* **32**, 773–785.
OISHI, C.M., THOMPSON, R.L. & MARTINS, F.P. 2019 Normal and oblique drop impact of yield-stress fluids with thixotropic effects. *J. Fluid Mech.* **876**, 642–679.
OLSSON, E. & KREISS, G. 2005 A conservative level set method for two phase flow. *J. Comput. Phys.* **210**, 225–246.
OSHER, S. & FEDKIW, R. 2001 Level-set methods: an overview and some recent results. *J. Comput. Phys.* **169**, 463–502.
OSHER, S. & SETHIAN, J.-A. 1988 Fronts propagating with curvature dependent speed: algorithms based on Hamilton–Jacobi formulations. *J. Comput. Phys.* **79**, 12–49.
PEREIRA, A., HACHEM, E. & VALETTE, R. 2020 Inertia-dominated coiling instabilities of power-law fluids. *J. Non-Newtonian Fluid Mech.* **282**, 104321.
PEREIRA, A., LARCHER, A., HACHEM, E. & VALETTE, R. 2019 Capillary, viscous, and geometrical effects on the buckling of power-law fluid filaments under compression stresses. *Comput. Fluids* **190**, 514–519.
QUÉRÉ, D. 2008 Wetting and roughness. *Annu. Rev. Fluid Mech.* **38**, 71–99.
QUETZERI-SANTIAGO, M.A., YOKOI, K., CASTREJON-PITA, A.A. & CASTREJON-PITA, R. 2019 Role of the dynamic contact angle on splashing. *Phys. Rev. Lett.* **122**, 1–6.
RAMÍREZ-SOTO, O., SANJAY, V., LOHSE, D., PHAM, J.T. & VOLLMER, D. 2020 Lifting a sessile oil drop from a superamphiphobic surface with an impacting one. *Sci. Adv.* **6**, 1–10.
REIN, M. 1993 Phenomena of liquid drop impact on solid and liquid surfaces. *Fluid Dyn. Res.* **12**, 61–93.
RIBER, S., VALETTE, R., MESRI, Y. & HACHEM, E. 2016 Adaptive variational multiscale method for Bingham flows. *Comput. Fluids* **138**, 51–60.
RICHARD, D., CLANET, C. & QUÉRÉ, D. 2002 Contact time of a bouncing drop. *Nature* **417**, 811.
ROISMAN, I.V., PRUNET-FOCH, B., TROPEA, C. & VIGNES-ADLER, M. 2002 Multiple drop impact onto a dry solid substrate. *J. Colloid Interface Sci.* **256**, 396–410.
RYU, S., SEN, P., NAM, Y. & LEE, C. 2017 Water penetration through a superhydrophobic mesh during a drop impact. *Phys. Rev. Lett.* **118**, 14501.
SOTO, D., GIRARD, H.-L., LE HELLOCO, A., BINDER, T., QUÉRÉ, D. & VARANASI, K.K. 2018 Droplet fragmentation using a mesh. *Phys. Rev. Fluids* **3**, 083602.
SU, M.-J., LUO, Y., CHU, G.-W., CAI, Y., LE, Y., ZHANG, L.-L. & CHEN, J.-F. 2020 Dispersion behaviors of droplet impacting on wire mesh and process intensification by surface micro/nano-structure. *Chem. Engng Sci.* **219**, 1–13.
VALETTE, R., HACHEM, E., KHALLOUFI, M., PEREIRA, A., MACKLEY, M.R. & BUTLER, S.A. 2019 The effect of viscosity, yield stress, and surface tension on the deformation and breakup profiles of fluid filaments stretched at very high velocities. *J. Non-Newtonian Fluid Mech.* **263**, 130–139.
VALETTE, R., PEREIRA, A., RIBER, S., SARDO, L., LARCHER, A. & HACHEM, E. 2021 Viscoplastic dam-breaks. *J. Non-Newtonian Fluid Mech.* **287**, 1–21.
VIJAYAVENKATARAMAN, S., YAN, W.-C., LU, W.F., WANG, C.-H. & FUH, J.Y.H. 2018 3D bioprinting of tissues and organs for regenerative medicine. *Adv. Drug Deliv. Rev.* **132**, 296–332.
VILLERMAUX, E. & BOSSA, B. 2011 Drop fragmentation on impact. *J. Fluid Mech.* **668**, 412–435.
WANG, G., FEI, L., LEI, T., WANG, Q. & LUO, K.H. 2022 Droplet impact on a heated porous plate above the Leidenfrost temperature: a lattice Boltzmann study. *Phys. Fluids* **34**, 093319.
WORTHINGTON, A.M. 1883 On impact with a liquid surface. *Proc. R. Soc. Lond.* **34**, 217–230.
YARIN, A.L. 2006 Drop impact dynamics: splashing, spreading, receding, bouncing …. *Annu. Rev. Fluid Mech.* **38**, 159–192.

https://doi.org/10.1017/jfm.2024.1164 Published online by Cambridge University Press